

Large Eddy Simulation of Reactive Two-Phase Flow in an Aeronautical Multipoint Burner

Gregory Hannebique · Patricia Sierra ·
Eleonore Riber · Bénédicte Cuenot

Received: 21 February 2012 / Accepted: 21 September 2012 / Published online: 9 October 2012
© Springer Science+Business Media Dordrecht 2012

Abstract Because of compressibility criteria, fuel used in aeronautical combustors is liquid. Their numerical simulation therefore requires the modeling of two-phase flames, involving key phenomena such as injection, atomization, polydispersion, drag, evaporation and turbulent combustion. In the present work, particular modeling efforts have been made on spray injection and evaporation, and their coupling to turbulent combustion models in the Large Eddy Simulation (LES) approach. The model developed for fuel injection is validated against measurements in a non-evaporating spray in a quiescent atmosphere, while the evaporation model accuracy is discussed from results obtained in the case of evaporating isolated droplets. These models are finally used in reacting LES of a multipoint burner in take-off conditions, showing the complex two-phase flame structure.

Keywords Large Eddy Simulation · Two-phase flow · Evaporation · Injection · Combustion · Multipoint burner

1 Introduction

Large Eddy Simulation (LES) is a powerful tool to simulate industrial-scale burners and to understand complex unsteady phenomena such as combustion instabilities, ignition or quenching, giving access to the large scales structures and reducing the importance of modeling [1–6]. Since many combustion systems burn liquid fuel, extending LES to spray flames is crucial but still challenging, mainly because the physical submodels required to describe the atomization of a liquid fuel jet [7, 8], the dispersion of fuel droplet, their interaction with walls [9], evaporation [10] and combustion [11–15] are essentially subgrid phenomena. Direct simulation using interface tracking methods [16–18] is promising but still unaffordable in complex

G. Hannebique (✉) · P. Sierra · E. Riber · B. Cuenot
CERFACS, 42 avenue Gaspard Coriolis, 31057 Toulouse Cedex 01, France
e-mail: hannebiqu@cerfacs.fr

geometries. Therefore, Euler–Euler and Euler–Lagrange approaches are widely used to perform LES in complex geometries [19–21].

The goal of this study is to present different models used to simulate liquid phase, and validate them against experiments. First, the liquid injection model is tested in a laminar case and compared to experiment. Then, a new evaporation model is described and validated in the configuration of a single isolated droplet evaporating in quiescent atmosphere. Finally, these models are used in a LES of a multipoint burner where the main phenomena to simulate a turbulent two phase flow flame are taken into account: injection, evaporation, turbulence and chemistry. The objective is to show the ability of the code to perform multiphysic simulations in complex geometries in critical conditions (take-off conditions), and to show the impact of liquid fuel on flame structure.

2 System Equations

2.1 Gas phase

The unstructured LES code AVBP explicitly solves the filtered compressible conservation equations for velocity u , total energy E and species mass fractions Y_k :

$$\frac{\partial}{\partial t} \bar{\rho} \tilde{u}_i + \frac{\partial}{\partial x_j} (\bar{\rho} \tilde{u}_i \tilde{u}_j) = - \frac{\partial}{\partial x_j} [\bar{p} \delta_{ij} - \bar{\tau}_{ij} - \bar{\tau}_{ij}^{sgs}] + \bar{s}_{mo,i} \quad (1)$$

$$\frac{\partial}{\partial t} \bar{\rho} \tilde{E} + \frac{\partial}{\partial x_j} (\bar{\rho} \tilde{u}_j \tilde{E}) = - \frac{\partial}{\partial x_j} (\tilde{u}_i (\bar{p} \delta_{ij} - \bar{\tau}_{ij}) + \bar{q}_j + \bar{q}_j^{sgs}) + \bar{s}_{en} \quad (2)$$

$$\frac{\partial}{\partial t} \bar{\rho} \tilde{Y}_k + \frac{\partial}{\partial x_j} (\bar{\rho} \tilde{u}_j \tilde{Y}_k) = - \frac{\partial}{\partial x_j} (\bar{J}_{j,k} - \bar{J}_{j,k}^{sgs}) + \bar{s}_{ms,k} \text{ for } k = 1, N \quad (3)$$

where $\bar{\cdot}$ states for the Reynolds spatial filtering and $\tilde{\cdot}$ states for the Favre spatial filtering: $\bar{\rho} \tilde{f} = \bar{\rho} \tilde{f}$. Einstein's summation convention is applied over repeated indices and δ_{ij} denotes the Kronecker symbol. The inter-phase exchange terms of momentum, energy and mass respectively, \bar{s}_{mo} , \bar{s}_{en} and $\bar{s}_{ms,k}$, are detailed in Section 2.3.2. $\bar{\tau}_{ij}$ stands for the laminar filtered stress tensor. The diffusive species flux $\bar{J}_{i,k}$ is evaluated with the Hirschfelder and Curtis approximation [22], a correction diffusion velocity V^c being added to ensure mass conservation [23]. The heat flux \bar{q}_j takes into account temperature diffusion as well as enthalpy flux due to differential species diffusion following Fouriers law. For the subgrid unclosed terms, the classical eddy-viscosity assumption is made:

$$\bar{\tau}_{ij}^{sgs} = \bar{\rho} (\tilde{u}_i \tilde{u}_j - \tilde{u}_i \tilde{u}_j) \approx 2 \bar{\rho} \nu_t \left(\tilde{S}_{ij} - \frac{1}{3} \delta_{ij} \tilde{S}_{kk} \right) \quad (4)$$

$$\bar{J}_{i,k}^{sgs} = - \bar{\rho} (\tilde{u}_j \tilde{Y}_k - \tilde{u}_j \tilde{Y}_k) \approx - \bar{\rho} \left(D_t \frac{W_k}{W} \frac{\partial \tilde{X}_k}{\partial x_j} - \tilde{Y}_k \tilde{V}_i^c \right) \quad (5)$$

$$\bar{q}_i^{sgs} = - \bar{\rho} (\tilde{u}_j \tilde{E} - \tilde{u}_j \tilde{E}) \approx - \lambda_t \frac{\partial \tilde{T}}{\partial x_j} + \sum_{k=1}^N \bar{J}_{i,k}^{sgs} \tilde{h}_{s,k} \quad (6)$$

The turbulent viscosity is computed with the Wall Adapting Local Eddy-viscosity model [24], which recovers the right scaling of turbulent viscosity close to solid boundaries and yields reduced damping in zones of pure shear compared to the standard Smagorinsky model [25]. The turbulent diffusive coefficients D_t and λ_t are computed from the turbulent viscosity and the turbulent Schmidt and Prandtl numbers both equal to 0.6: $D_t = m_t/Sc_t$ and $\lambda_t = \bar{\rho}_t \bar{C}_p/Pr_t$.

2.2 Dispersed liquid phase

The spray is here assumed diluted, which means that the maximum liquid volume fraction is low enough to neglect collisions. The droplets are much smaller than the LES filter width, allowing the point source approximation. Moreover, droplet deformation effects are small, motion due to shear is negligible and gravitational effects are not significant compared to drag.

The mesoscopic Eulerian approach used in this work describes the dispersed phase with ensemble average of the droplet properties over a given set of liquid-phase realizations, conditioned on one gas-phase realization and denoted $\tilde{\cdot} = \langle \cdot | \mathcal{H}_f \rangle$. The continuous averaged properties—also called mesoscopic quantities—are for a monodisperse evaporating spray: the droplet number density \tilde{n}_l , the liquid volume fraction $\tilde{\alpha}_l$, the velocity \tilde{u}_l and the enthalpy \tilde{h}_l . Each statistic droplet sample is described by a single diameter d defined by $\tilde{\alpha}_l = \tilde{n}_l \pi d^3/6$. With these definitions the discrete drop velocity u_p may be separated into an Eulerian part, the mesoscopic velocity \tilde{u}_l and a Lagrangian random part, the random uncorrelated velocity u_p'' [26]:

$$u_p = \tilde{u}_l + u_p'' \quad (7)$$

This random motion affects the distribution of droplets and is enhanced in zones of high shear and compressibility of the mesoscopic motion. This effect can be taken into account by solving a transport equation for the associated kinetic energy [27]. In this work however it is neglected, following the results of [28] where it was shown that neglecting random motion introduces error on fluctuations only, still leading to a correct prediction of the mean flow. By analogy with the gas phase Favre filtering, a LES filter is applied to the mesoscopic equations $\tilde{\alpha}_l \tilde{f}_l = \bar{\alpha}_l \hat{f}_l$ where $\bar{\alpha}_l = \tilde{\alpha}_l$ is the spatially filtered liquid volume fraction. The subgrid velocity modelling accounts only for the mesoscopic motion. The final set of filtered equations for the dispersed phase is summarized below [29].

$$\frac{\partial \tilde{n}_l}{\partial t} + \frac{\partial \tilde{n}_l \hat{u}_{l,j}}{\partial x_j} = 0 \quad (8)$$

$$\frac{\partial \rho_l \bar{\alpha}_l}{\partial t} + \frac{\partial \rho_l \bar{\alpha}_l \hat{u}_{l,j}}{\partial x_j} = -\bar{\Gamma} \quad (9)$$

$$\frac{\partial \rho_l \bar{\alpha}_l \hat{u}_{l,i}}{\partial t} + \frac{\partial \rho_l \bar{\alpha}_l \hat{u}_{l,i} \hat{u}_{l,j}}{\partial x_j} = -\bar{F}_{d,i} - \hat{u}_{l,i} \bar{\Gamma} - \frac{\partial}{\partial x_j} \left(-\bar{\tau}_{l,ij}^{sgs} \right) \quad (10)$$

$$\frac{\partial \rho_l \bar{\alpha}_l \hat{h}_l}{\partial t} + \frac{\partial \rho_l \bar{\alpha}_l \hat{u}_{l,j} \hat{h}_l}{\partial x_j} = -\hat{h}_l \bar{\Gamma} + \bar{\Phi}_l \quad (11)$$

where the subgrid diffusion term of liquid enthalpy is neglected.

The filtered drag-force contribution is written \bar{F}_d , the filtered evaporation rate is denoted $\bar{\Gamma}$. $\bar{\Phi}_l$ is the filtered average of the conductive heat flux on the liquid side at the droplet surface. Details on the source terms are provided in Section 4. $\bar{\tau}_l^{sgs}$ is the droplet subgrid stress tensor, modeled by analogy to compressible single-phase flows, using a Smagorinsky formulation for the trace- free part together with a Yoshizawa formulation for the trace part [29]:

$$\bar{\tau}_{l,ij}^{sgs} = -\rho_l \bar{\alpha}_l \left(-C_s^2 \Delta^2 ||\hat{S}_l^*|| \hat{S}_{l,ij}^* + C_Y \Delta^2 ||\hat{S}_l^*||^2 \delta_{ij} \right) \quad (12)$$

$$\text{with: } \hat{S}_{l,ij}^* = \left(\frac{\partial \hat{u}_{l,i}}{\partial x_j} + \frac{\partial \hat{u}_{l,j}}{\partial x_i} \right) - \frac{2}{3} \frac{\partial \hat{u}_{l,k}}{\partial x_k} \delta_{ij} \quad (13)$$

$$||\hat{S}_l^*|| = \frac{1}{2} \hat{S}_{l,ij}^* \hat{S}_{l,ij}^* \quad (14)$$

2.3 Phase exchange terms

2.3.1 Drag force

Considering spherical droplets and high particle-to-fluid density ratio ($\rho/\rho_l \ll 1$) without gravity, the Stokes drag force is used with the correction of Schiller and Naumann [30], accounting for non zero relative velocity:

$$\bar{F}_{d,i} = \frac{\rho_l \bar{\alpha}_l}{\tau_p} (\hat{u}_{l,i} - \tilde{u}_i) \text{ with: } \tau_p = \frac{\rho_l d^2}{18\mu} \frac{1}{1 + 0.15 Re_p^{0.687}} \quad (15)$$

where Re_p is the particle Reynolds number.

2.3.2 Evaporation and gaseous source terms

The evaporation model proposed in this work is detailed in Section 4. The source terms $\bar{s}_{mo,i}$, \bar{s}_{en} and $\bar{s}_{ms,k}$ in the gas phase in Eqs. 1, 2 and 3 are:

$$\bar{s}_{mo,i} = \bar{\Gamma} \hat{u}_{l,i} - \bar{F}_{d,i} \quad (16)$$

$$\bar{s}_{en} = -\bar{\Phi}_l + \hat{h}_l \bar{\Gamma} + \bar{\Gamma} \left(\frac{1}{2} \hat{u}_{l,i}^2 \right) - \hat{u}_{l,i} \bar{F}_{d,i} \quad (17)$$

$$\bar{s}_{ms,k} = \bar{\Gamma} \delta_{kF} \quad (18)$$

2.4 Numerics

The gas and liquid flow equations are solved with an optimized Two-step Taylor-Galerkin scheme (TTGC) which achieves third order accuracy in time and space for convective terms [31]. Inlet and outlet boundary condition treatment use a one-dimensional formulation for non reflecting characteristic boundary conditions for viscous flows [32]. For liquid boundary conditions, Dirichlet conditions are used.

3 Liquid Injection Modeling Using the FIM-UR Approach

In many aeronautical burners, the spray is generated by an air-blast atomizer, and is the result of complex processes, initiated inside the injector itself and involving

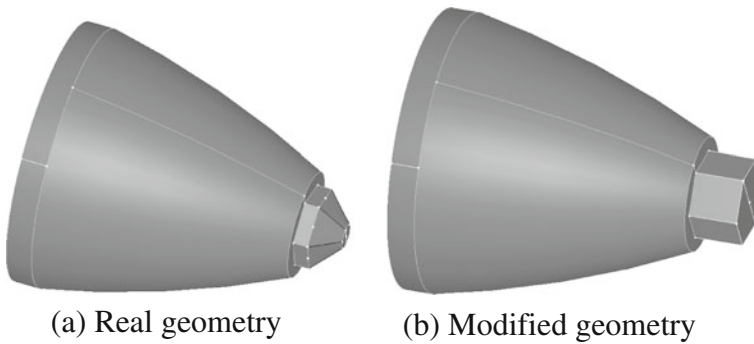
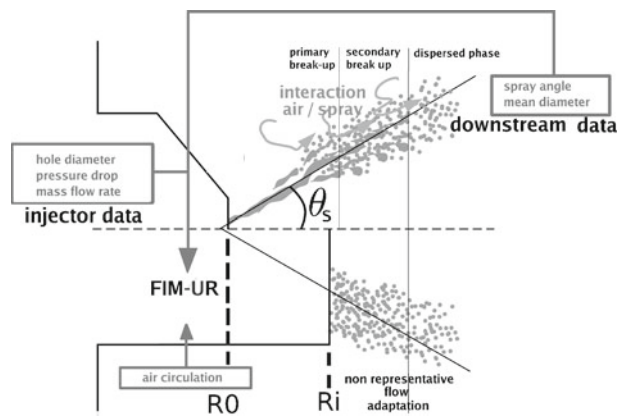


Fig. 1 Geometric modification implied by the FIM-UR model in the Eulerian approach for the dispersed phase

interaction with the air flow [33]. The liquid jet exiting from the injector is first submitted to strong shear from the air flow leading to primary atomization. In a second phase, secondary atomization occurs through interactions with the air and between droplets. In the same time, drag force and evaporation modify the gas flow and composition in the spray. Simulating primary atomization is a challenging and still open problem [16–18], which requires the description of liquid/gas interface, and is today out of reach in LES of complex two-phase reacting flows. The FIM-UR model (for **F**uel **I**njection **M**ethod by **U**pstream **R**econstruction) proposed in [21] circumvents the atomization issue by building from global and geometrical characteristics the profiles of the liquid volume fraction, gas and liquid velocity and droplet size at the close vicinity of the injector. This model was already successfully tested in a swirled turbulent configuration [21]. To better assess the accuracy of the model, it is here tested on the simple laminar configuration of [34], where the injection system is isolated from other physical phenomena. In particular the impact of injector geometry modification, consisting in increasing the injection surface to avoid high liquid volume fraction and stay in the dilute spray hypothesis (see Fig. 1), is evaluated.

Fig. 2 Principle of the FIM-UR model



The input parameters are the initial injection diameter ($2 * R_0$), the mass flow rate, the droplet mean diameter, the spray angle, and the modified geometry. Figure 2 gives a global picture of the model.

The principle of FIM-UR is to build profiles of the various spray quantities that allow to recover the correct flow downstream. At the real injection surface of radius R_0 , the axial liquid velocity is supposed uniform, the radial component is zero and the tangential component increases linearly from zero at the center to a maximum at the solid boundary of the injector, to mimic the rotation motion induced by this type of atomizer (Fig. 3a). This motion leads to the creation of an air core in the center of the injector, modeled here by a zero liquid volume fraction in this zone, while it is unity in the liquid sheet. As unity liquid volume fraction is not supported by

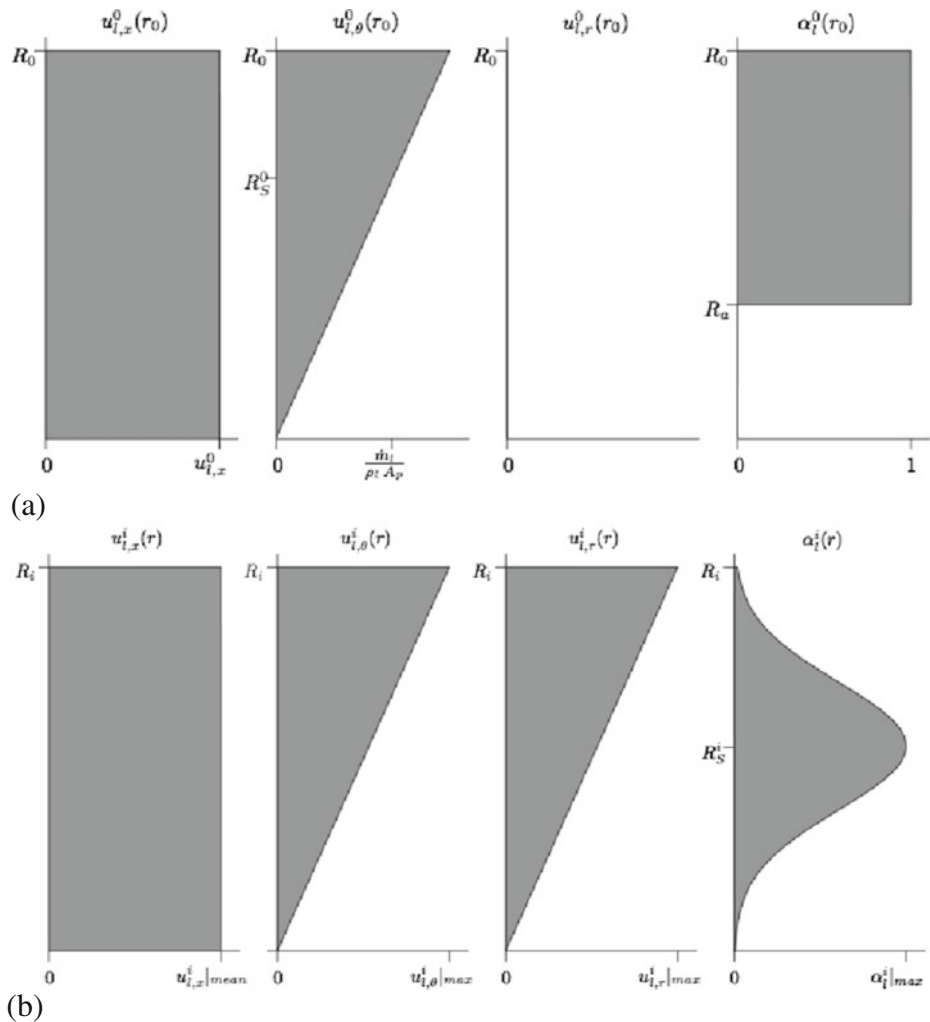


Fig. 3 Profiles of liquid axial, tangential, radial components of velocity, and liquid volume fraction: at the real injection plane (a), and at the numerical injection plane (b)

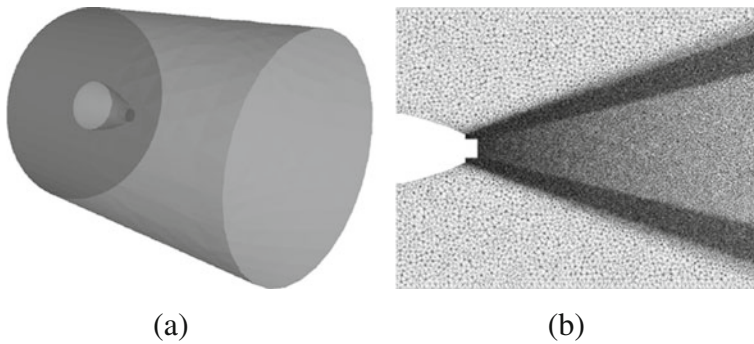


Fig. 4 Injection test case for FIM-UR **a** geometry **b** mesh

the two-phase flow model, the injection plane is enlarged to a radius R_i and moved downstream in the simulation, at a location where the liquid volume fraction has sufficiently decreased (Fig. 2). Applying momentum conservation and including the interaction with air, profiles at this numerical injection plane are derived: the radial component is here linear also, and a gaussian profile for the liquid volume fraction is used to represent the hollow cone shape of the spray (Fig. 3b).

The test configuration is a simple cylindrical chamber with a pressure-swirl Delavan atomizer injecting kerosene in a quiescent atmosphere. Initial gas and liquid temperatures are both 300 K. The spray is assumed monodisperse with a droplet mean diameter of $55\ \mu\text{m}$. The half-spray angle is 30° . The mass flow rate is $3\ \text{g}\cdot\text{s}^{-1}$, and the orifice diameter R_0 is 0.5 mm. Figure 4a and b show the computational domain and a vertical mid-plane cut of the mesh, respectively. The mesh is composed of 3.5 million nodes and 20 million cells. 10 ms of physical time was simulated to reach a stationary flow, then averaging was done over 15 ms.

Figure 5 shows a qualitative comparison of the observed and computed sprays. The experimental direct visualization in Fig. 5a shows a half-spray angle of 30° degrees. This angle as well as the spray penetration are well reproduced in the computed spray, as shown in Fig. 5b. The hollow cone structure is also well reproduced.

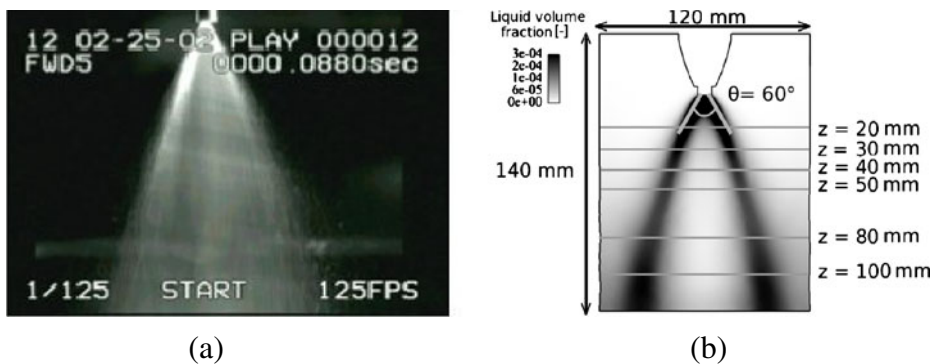
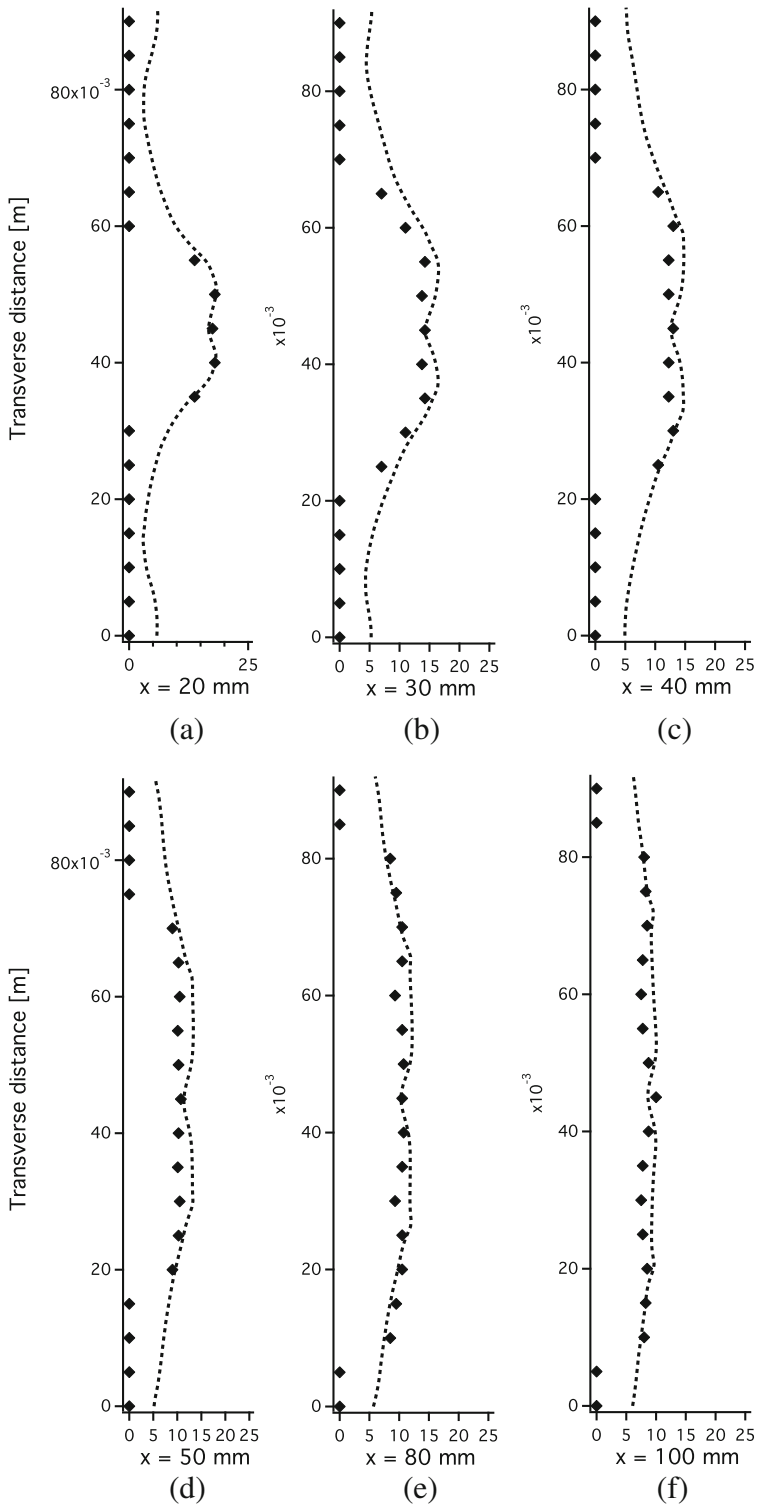


Fig. 5 Injection test case for FIM-UR: **a** experimental direct visualization **b** mean liquid volume fraction field in the mid-plane from simulation



◀ **Fig. 6** Injection test case for FIM-UR: radial profiles of mean liquid axial velocity at various stations downstream of the injector nozzle. Comparison between experiment (*black diamonds*) and simulation (*dashed lines*)

This indicates that the FIM-UR injection model correctly sets the liquid velocity and volume fraction and that the monodisperse assumption is acceptable in this case. To better assess the validity of the model, mean liquid axial velocity profiles obtained from the LES are compared to the measurements in Fig. 6 at various axial distances from the injector nozzle, indicated in Fig. 5b. The overall shape and level are in good agreement with the experimental results. Droplets are slowed by the gas phase, although far from the tip.

4 Evaporation Modeling

The evaporation model used in this work (referred hereafter as ‘AVBP-standard’) assumes infinite conduction in the liquid and spherical symmetry of the droplet. The gas is considered quasi-stationary, so that thermal and mass transfers in the gas phase only depend on the distance to the surface of the droplet [19]. Until recently, all experiments measuring the diameter temporal evolution of an evaporating isolated droplet were conducted with the droplet suspended on a support fiber to avoid the experimental difficulty of free-falling droplets [35]. Chauveau et al. [36] however proposed recently to use a novel cross micro-fiber system in order to reduce the diameter of the fiber and consequently the effect of heat conduction through the fiber, while keeping the spherical shape of the droplet. Repeating the experiment from the literature of a n-heptane droplet evaporating in a N_2 quiescent atmosphere, the evaporation time was almost doubled. In parallel, simulation of the same experiment by Sanjosé [37] showed that the evaporation process is strongly influenced by the modeling of the mixture thermodynamic properties at the droplet surface. Based on this last observation, a new evaporation model [38], referred hereafter as ‘AVBP-mix’ model, is proposed here and compared both to the ‘AVBP-standard’ model and to experiments [35, 36].

The Abramzon–Sirignano approach [39] is used to compute the mass transfer rate Γ and the heat transfer due to phase exchange, composed of two contributions, the conductive flux Φ_g and the enthalpy flux Λ_g :

$$\Gamma = -\pi d Sh [\rho D_F] \ln(1 + B_M), \quad (19)$$

$$\Phi_g = -\pi d Nu \lambda (T_{\text{inf}} - T_l) \frac{\ln(1 + B_T)}{B_T}, \quad (20)$$

$$\Lambda_g = \Gamma h_{s,F}(T_l), \quad (21)$$

In the above equations, Sh and Nu are respectively the Sherwood and the Nusselt numbers following the Ranz–Marshall correlations [40], D_F is the fuel diffusivity, $B_M = (Y_{F,\zeta} - Y_{F,\text{inf}}) / (1 - Y_{F,\zeta})$ is the Spalding mass number, $B_T = (1 + B_M)^\beta$ is the thermal Spalding number ($\beta = C_{p,F}/C_p \times Sh \cdot Pr/Nu \cdot Sc$, where $C_{p,F}$ stands for the gaseous fuel heat capacity, and C_p is the heat capacity of the mixture, and Pr and Sc are the mixture Prandtl and Schmidt numbers). Subscript ζ indicates droplet surface properties and $Y_{F,\zeta}$ is calculated using the Clausius–Clapeyron law.

Thermodynamic and transport properties are computed using the reference state corresponding to the 1/3 law [41] which assumes that the properties in the gaseous film surrounding the droplet follow a quasi-stationary evolution. The ‘AVBP-standard’ and ‘AVBP-mix’ models differ in the way these thermodynamic and transport properties are calculated. In the ‘AVBP-standard’ model, the mixture Prandtl and Schmidt numbers at the droplet surface are taken equal to those in the gas flow. Moreover, the product $[\rho D_F]$ is considered constant from the droplet surface to infinity and is written as:

$$[\rho D_F] = \frac{\mu(T_{\text{ref}})}{Sc_F}, \quad (22)$$

where Sc_F is the fuel Schmidt number, T_{ref} is the reference temperature and μ is the mixture viscosity. Note that assuming $[\rho D_F]$ and Sc_F constant leads to a dynamic viscosity $\nu = \mu/\rho$ proportional to T , which is close to classical power law for this quantity.

There are two improvements in the ‘AVBP-mix’ model. First, the Prandtl and Schmidt numbers of the mixture at the droplet surface are deduced from complex calculations using the CANTERA software [42], and are more realistic. Second, the mixture viscosity still evaluated at the reference temperature also depends now on mixture composition following the Wilke relation [43]:

$$\mu = \sum_i \frac{X_i \mu_i}{\sum_j X_j \Phi_{ij}}, \quad (23)$$

$$\Phi_{ij} = \frac{1}{\sqrt{8}} \left(1 + \frac{W_i}{W_j}\right)^{-1/2} \left[1 + \left(\frac{\mu_i}{\mu_j}\right)^{1/2} \left(\frac{W_j}{W_i}\right)^{1/4}\right]^2, \quad (24)$$

where μ_i is the viscosity of species i in the gas mixture, fitted with power law of temperature on the CANTERA database.

The ‘AVBP-mix’ model is now close to the Chapman–Enskog kinetic theory of gases (used in CANTERA). the remaining differences are the species diffusion coefficients which depend on the binary diffusion coefficients, and the thermal conductivity of the mixture which is a combination of the thermal conductivity of each species in the mixture. To assess the accuracy of the ‘AVBP-mix’ evaporation model, comparison with the kinetic theory in academic configurations was performed. To do that, the LES code was coupled to CANTERA to build a third model called the ‘AVBP–CANTERA’ model, and used as reference.

Table 1 details the initial conditions for two cases of isolated droplet evaporating in a quiescent atmosphere. Case 1 corresponds to the academic case of [35] repeated in [36] whereas Case 2 corresponds to the evaporation conditions of a kerosene droplet outing from the pilot injection of the multipoint burner configuration

Table 1 Initial conditions for the simulation of isolated droplet evaporating in a quiescent atmosphere

	Fuel	Gas	Pressure [atm]	Gas temperature [K]	Droplet temperature [K]	Droplet diameter [μm]
Case 1	n-heptane	N ₂	1	623	300	500
Case 2	kerosene	air	19	728	300	10

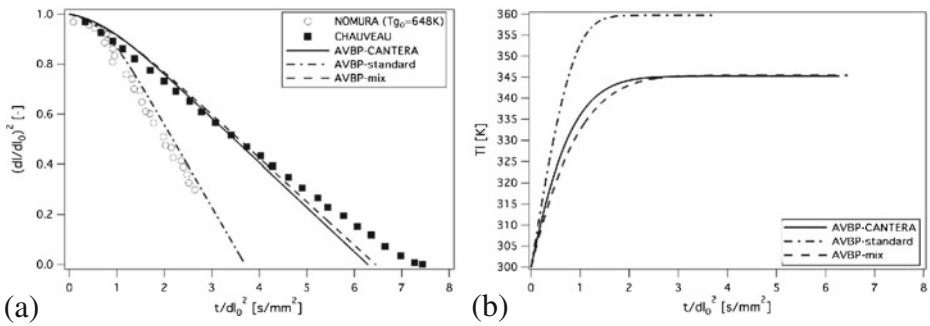


Fig. 7 Temporal evolution of squared droplet diameter **(a)** and liquid temperature **(b)** for Case 1 in Table 1. Comparison between measurements [35, 36] and simulations using ‘AVBP-standard’, ‘AVBP-mix’ and ‘AVBP-CANTERA’ models

presented in Section 5. Figure 7 shows the temporal evolution of the squared droplet diameter and temperature for Case 1, as obtained with the three models and compared to measurements (for diameter only). It clearly appears that the transport and thermodynamic properties used in the evaporation model considerably affect the evaporation time: ‘AVBP-mix’ doubles the evaporation time in comparison to ‘AVBP-standard’, and is close to the measurements of Chauveau et al. [36]. The comparison between ‘AVBP-mix’ and ‘AVBP-CANTERA’ shows that the modified mixture properties of ‘AVBP-mix’ are sufficient to correctly reproduce evaporation. In addition, the evaporation model has a non-negligible impact on the liquid temperature, as displayed in Fig. 7b. The same behaviour is observed for the droplet of kerosene in Case 2 (Fig. 8), for which the only available reference is the ‘AVBP-CANTERA’ result. Results show that the ‘AVBP-standard’ model still fails to predict both the evaporation time, and the equilibrium liquid temperature, whereas the new evaporation ‘AVBP-mix’ model performs well on both quantities and appears sufficiently accurate to be applied to a real combustor.

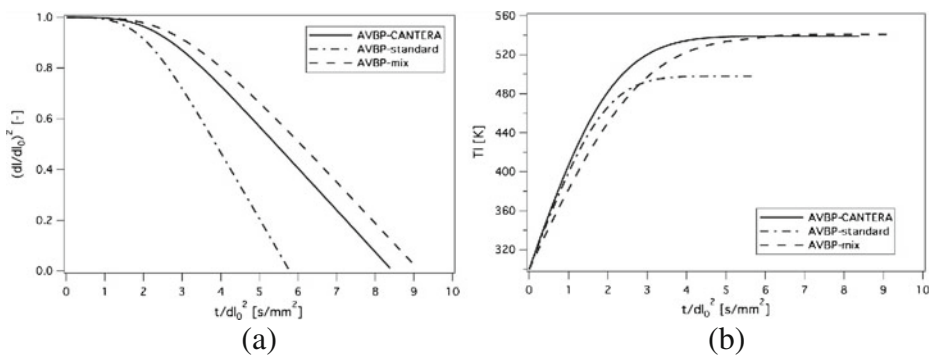


Fig. 8 Temporal evolution of squared droplet diameter **(a)** and liquid temperature **(b)** for Case 2 in Table 1. Comparison between simulations using ‘AVBP-standard’, ‘AVBP-mix’ and ‘AVBP-CANTERA’ models

5 Application to the Multipoint Injection Burner

The multipoint injection burner was set-up in the framework of the TLC (Towards Lean Combustion) European Project and is representative of a real industrial burner, where liquid fuel is injected by both a pilot and a series of liquid jets distributed around it, while air is swirled through a complex premixing swirler. The computational domain shown in Fig. 9 includes a multipoint injection system, a plenum for air supply, a chamber and an exit nozzle.

Details of the pilot and the multipoint fuel injectors are provided in Fig. 10a. The pilot fuel atomizer is of the piezo-type, and a series of 24 holes of diameter 0.5 mm, located around the inner wall of the main stage forms the multipoint injector. The fuel distribution among the two systems depends on the operation regime. The premixing swirler has three stages as shown in Fig. 10b. All stages are counter-rotating relative to each other, which increases the turbulent mixing in the areas where the different flows meet. Approximately 90 % of the total air goes through the main swirler stage. The remaining 10 % is split between the inner (3 %) and the outer pilot swirlers (7 %). Multiperforated walls are used to provide cooling air to the chamber. At the choked exit nozzle, supersonic flow conditions lead to acoustically non-reflecting outflow boundary condition.

The computed operating point corresponds to take-off conditions (full thrust), where both fuel injectors are fed with kerosene at temperature $T_l = 300$ K. Droplets with a diameter of 10 μm and a half spray angle of 30° are injected at the pilot injector nozzle using the FIM-UR model and account for 15 % of total injected kerosene, whereas droplets with a diameter of 30 μm are injected perpendicularly to the hole surface of the multipoint injector. Air is injected at temperature $T_g = 728$ K. The fuel/air ratio corresponds to a global equivalence ratio of 0.44. The chamber pressure is 19.5 bars.

The simulation was performed using the unstructured mesh illustrated in Fig. 11, composed of about 23.5 million cells and 4.2 million nodes. It is strongly refined in the mixing and reactive zones, around the swirlers and the injection systems. The same models and boundary conditions as for the laminar liquid injection simulation are used. Moreover, the 2S_KERO_BFER two-step reduced scheme for kerosene-air flames [44] is used. It accounts for a kerosene oxidation reaction and the CO-CO₂ equilibrium, and has been fitted against experimental data and detailed mechanisms to reproduce correctly the laminar flame speed and the burnt gas temperature over a wide range of pressure, temperature and equivalence ratio. The Dynamic Thickening flame model [45] is used to model flame-turbulence interactions.



Fig. 9 Computational domain for the multipoint injection burner

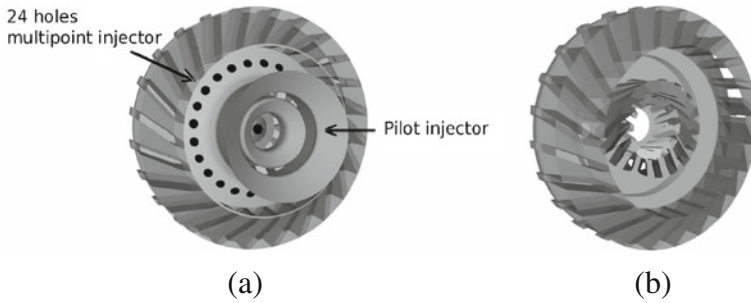


Fig. 10 Close view of the two injection systems **a** and the three swirler stages **b**

5.1 Results—cold flow

Figure 12a shows the gas mean axial velocity field in a vertical cut plane of the combustion chamber. Under the effect of swirl, the flow opens largely when entering the chamber and different recirculation zones appear: a central toroidal recirculation zone occupies a large volume of the chamber and enters into the diffuser of the injection system. Corner recirculation zones also develop in the upstream corners of the chamber. Strong shear layers appear in the regions where the flows issuing from the different stages meet, as shown by the gas fluctuating (RMS) axial velocity field in Fig. 12b. In these zones, the turbulence intensity reaches 25 %, leading to strong mixing. Validation of LES in the same geometry but for a smaller chamber pressure ($P = 4.37$ bars) was proposed in [46] by comparison with experiment.

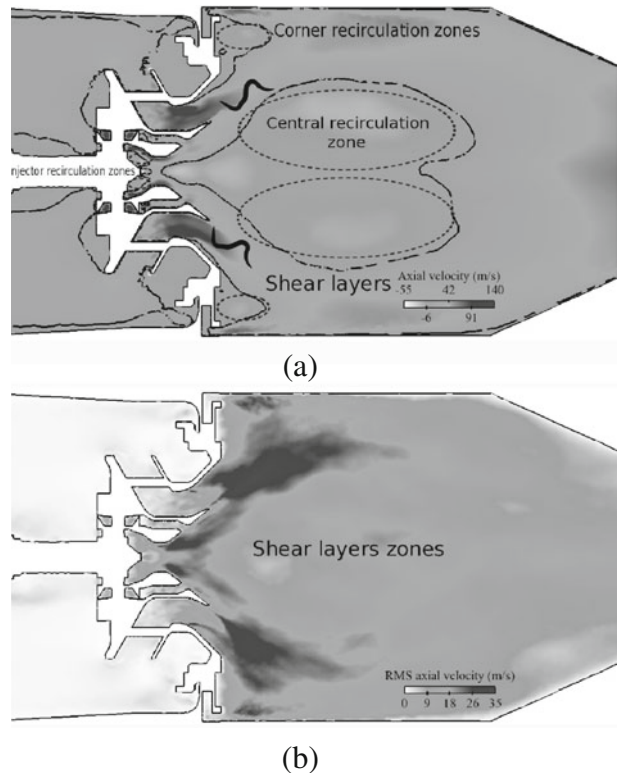
5.2 Results—reactive case

A global picture of the two-phase flame is given in Fig. 13 with the mean liquid volume fraction field and an isoline of heat release. It clearly shows how the liquid kerosene enters the chamber through both injection lines, follows the opening air flow and evaporates upstream and inside the flame front. A conical flame is obtained, stabilized by both injections and extending around the recirculation zone, in the high shear region. This flame produces hot gases at a temperature close to 2600 K (corresponding to the stoichiometric burnt gas temperature) that fill the central recirculation zone (Fig. 13b). These gases do not mix immediately with the surrounding cold flow, resulting in a quite inhomogeneous temperature distribution in the first half of the chamber. Mixing is however almost complete in the second half of the chamber, resulting in a significant decrease of the temperature at the chamber exit. Figure 13b also shows that in the second half of the chamber, *i.e.* in a well mixed region, the computed mean temperature profile is relatively flat, with a mean value

Fig. 11 Vertical mid-plane cut of the mesh used for the multipoint injection configuration



Fig. 12 Flow topology in the multipoint injection burner. **a** Mean gas axial velocity field in the vertical cut plane, with the zero-axial gas velocity isoline (black line). **b** RMS gas axial velocity field in the vertical cut plane



($T_{\text{mean}} = 1796\text{K}$) almost equal to the burnt gas temperature at the global equivalence ratio of the simulation ($T_{BG} = 1793\text{K}$) as expected.

The local flame structure depends on the spray dispersion and evaporation, resulting in a non-homogeneous field of kerosene vapor which in turn mixes with the ambient air. Figure 14a shows an instantaneous field of fuel vapor, together with an isoline of evaporation mass transfer (in grey) and an isoline of heat release (in black). Evaporation mainly occurs in the fresh gases close to the injector exit. In the present operation conditions, saturation is reached rapidly in the evaporating pilot spray and the time needed to evaporate all the liquid is about 1 ms, while the convective time needed to reach the flame is much smaller (0.225 ms). In addition, most of the droplets issued from the pilot are stopped by the central recirculation zone, where the flame stabilizes, and complete their evaporation there. As a consequence, evaporation also occurs in the flame and in the burnt gases. This is not the case for the droplets injected through the multipoint injector: even if saturation is reached rapidly next to injection, the liquid volume fraction decreases enough to enable evaporation, with a characteristic evaporation time close to 0.6 ms which is smaller than the convective time 0.7 ms. This leads to a complex flame structure, as will be seen later.

The liquid injections result then in a partially premixed flame, experiencing variable equivalence ratio. The small droplets issued from the central pilot evaporate fast enough to create a rich premixed flame in the close vicinity of the injector,

producing burnt gases without oxygen. The remaining droplets go through the flame, accumulate and evaporate just behind, leading to a high fuel vapor concentration in this region which mixes with the oxygen-free burnt gases. The liquid injected by the multipoint system being more diluted when reaching the flame, gives smaller equivalence ratio. The resulting field of mixture fraction Z is shown in Fig. 14c where isolines of temperature are superimposed. Note that Z is based on the C atom as:

$$Z = \frac{Y_C - Y_C^O}{Y_C^F - Y_C^O}, \quad (25)$$

where Y_C is the mass fraction of the C atom, and the superscripts O and F refer to the pure oxidizer and pure fuel streams respectively. In the present case, $Y_C^O = 0$ and the mixture fraction reduces to $Z = Y_C/Y_C^F$, varying from 0 in pure air to 1 in pure kerosene. The stoichiometric value is $Z_{st} = 0.0625$. As diluted kerosene sprays are injected in the present configuration, the liquid volume fraction, even at the injector, stays far from unity. As a consequence, the maximum value of Z obtained in the calculation does not exceed 0.2. The mixture fraction gradually increases from the injectors downstream of the flame, and continues to increase in the burnt gases behind the flame in the tip region of the central recirculation zone, while it stays close to stoichiometry or below in the rest of the chamber, where it finally goes back to the global value of 0.02625. Interestingly, the flame follows the stoichiometric isoline as long as it exists in the fresh reactants. This is the consequence of the variable

Fig. 13 Multipoint injection burner: **a** Mean liquid volume fraction field in the vertical mid-plane cut, with mean heat release isoline (black line, value $4.6 \times 10^9 \text{ J/m}^3/\text{s}$). **b** Mean gas temperature in the vertical mid-plane cut with radial profile of mean temperature compared to the burnt gas temperature at global equivalence ratio $\phi = 0.44$

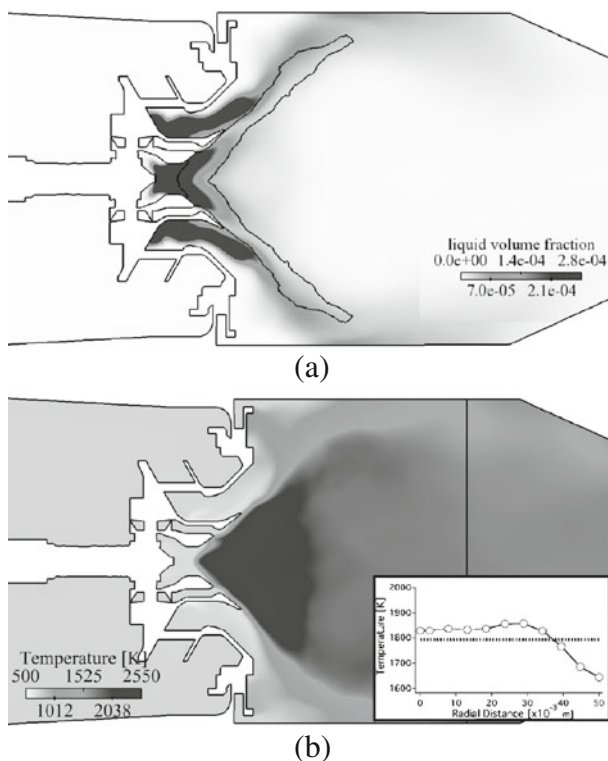
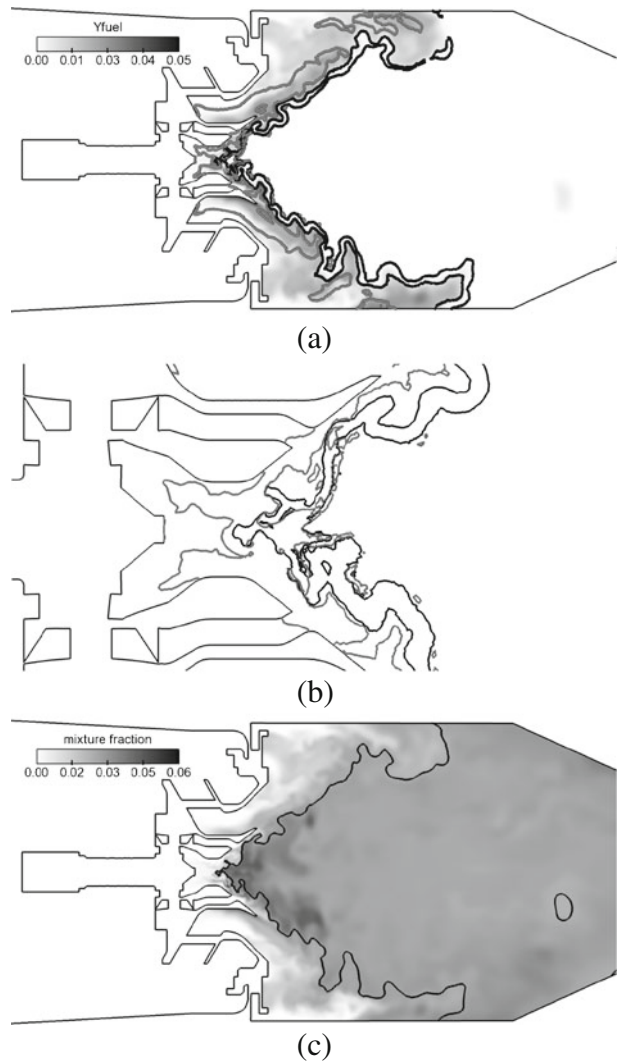


Fig. 14 Multipoint injection burner: **a** Instantaneous fuel vapor field in the vertical mid-plane cut, with isolines of heat release (*black line*) and evaporation mass transfer (*grey line*), **b** Zoom on the zone next to the injector, **c** Instantaneous mixture fraction field in the vertical mid-plane cut, with black isoline of temperature $T = 1500\text{K}$



equivalence ratio through the flame, due to evaporation, and leading to a maximum heat release at stoichiometry. Note also that the downstream parts of the flame front burn at an equivalence ratio close to the lean flammability limit ($\phi = 0.4$).

To understand the flame structure, the Takeno index [47] was calculated to identify the local combustion regimes. As a reminder, Takeno index is defined as:

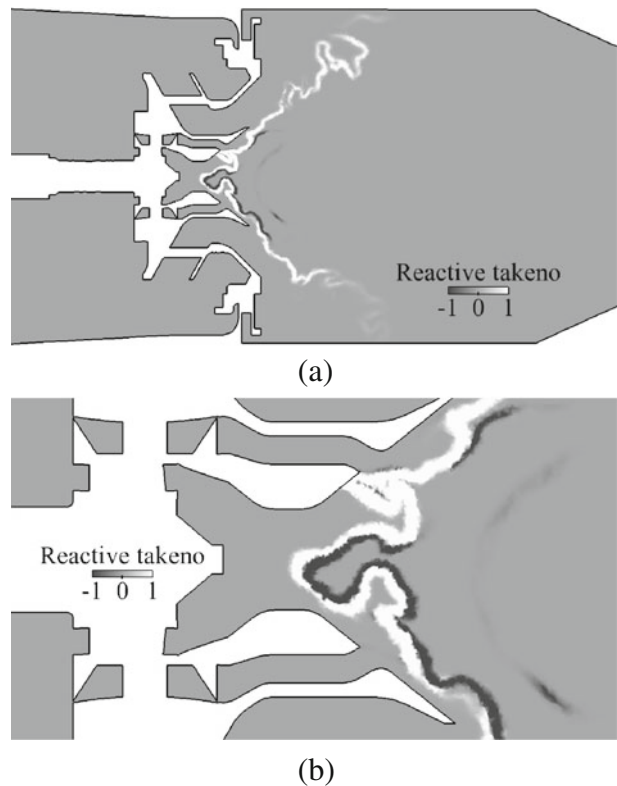
$$\text{Takeno} = \nabla Y_F \cdot \nabla Y_O \quad (26)$$

where Y_F is the mass fraction of fuel and Y_O is the mass fraction of oxydizer. Such a product of gradients enable to characterize combustion regimes: positive values indicate premixed regime, while negative values are found for diffusion flames. The Takeno index is then normalized to be 1 in premixed flames and -1 in diffusion

flames, and is conditioned on the reaction zone. Results are displayed in Fig. 15. They reveal a diffusion flame downstream of the main premixed flame, which was too weak to be visible in the previous pictures. This flame is the result of the burning of the very rich, oxygen-free burnt gas pocket generated by the pilot spray evaporation, with the oxygen remaining in the burnt gases and possibly coming from the external swirler stage, in a fully non-premixed regime. Otherwise the whole flame is premixed, with variable equivalence ratio. A particular structure is also revealed by the change of sign of the Takeno index in the burnt side of the flame: this is due to the change of sign of the fuel vapor gradient, which increases again under the effect of spray evaporation. In this zone, although the Takeno index is negative, the combustion regime is still premixed, with a variable equivalence ratio across the flame.

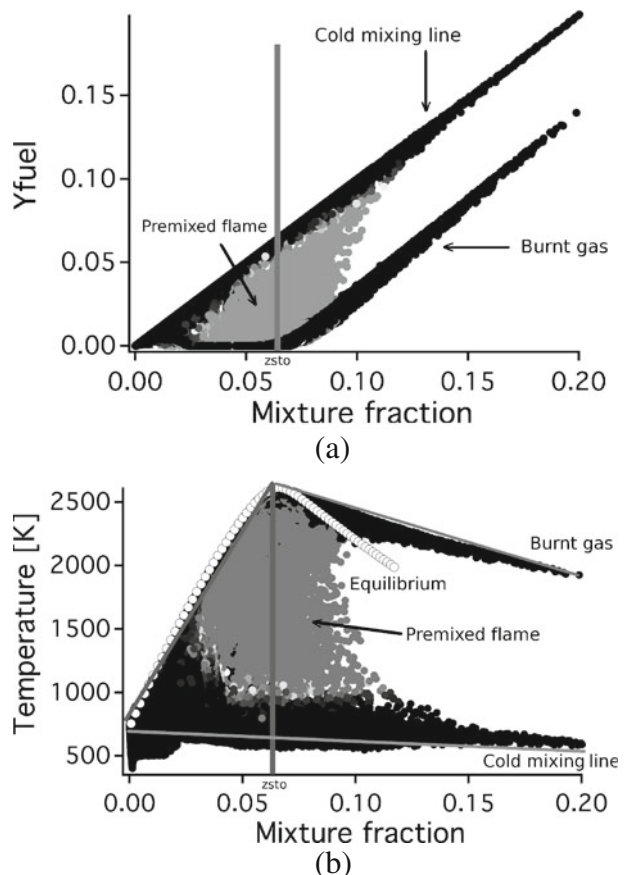
This particular structure is characterized in Fig. 16a and b with scatterplots of fuel vapor and temperature versus mixture fraction respectively. Dots are colored by the Takeno index, and in Fig. 16b, the chemical equilibrium solution for purely gaseous mixtures is plotted with white symbols as a reference. In both figures, classical limits are found and are drawn with lines. The first one corresponds to the non-reacting mixing of air at 728K with fuel vapor at the equilibrium temperature 560K, and is described by the line $Y_F = Z$ in Fig. 16a and the bottom line in Fig. 16b. Note that some temperatures lie below this bottom line as the injected air is slightly cooled by the evaporation process in the unburnt mixture. The second limit describes fully

Fig. 15 Multipoint injection burner: **a** Instantaneous field of normalized and reaction-conditioned Takeno index. **b** Zoom on the injection region



burnt gases, and is materialized by the bottom lines in Fig. 16a and upper lines in Fig. 16b. In the fuel mass fraction scatter plot of Fig. 16a, this limit corresponds to the infinitely fast chemistry, diffusion flame structure between pure air and fuel diluted in burnt gases, i.e. two line portions joining at the stoichiometric point. However in the temperature scatter plot of Fig. 16b, this diffusion flame structure lies above the gaseous equilibrium temperature on the rich side. This might be surprising as one would expect that the introduction of liquid fuel would lower the maximum temperature due to evaporation. In fact it describes the secondary purely diffusion flame revealed by the Takeno index, that occurs in burnt gas and is fed by the evaporation of fuel droplets in this region. As a consequence, on the rich side, the mixture fraction increases without significant change of the temperature, moving burnt gas points towards richer mixtures. These fuel-enriched mixture then burns with oxydizer in a purely diffusion flame, creating the upper limit of Fig. 16b. Between the non reacting and diffusion flame limits, a large region is filled with grey dots corresponding to the premixed flame with varying equivalence ratio. A small zone just above the non-reacting mixing line is filled with dark points, representing the pre-heating and mixing with burnt gases of the non-homogeneous mixture of air

Fig. 16 Multipoint injection burner: scatter plots of **a** the fuel vapor mass fraction, and **b** the gas temperature versus mixture fraction, colored by the Takeno index (*grey dots*: positive Takeno index; *black dots*: negative Takeno index). *White symbols* represent chemical equilibrium of gaseous mixtures



and kerosene vapor just in front of the flame. The premixed flame burns locally in the mixture fraction range $Z \in [0.03; 0.1]$, i.e. $\phi \in [0.5; 1.5]$, higher than the global equivalence ratio of 0.44 and around stoichiometry. This demonstrates that the multipoint injection burner allows to stabilize a flame even at a very lean global equivalence ratio, which is the main objective of such design. The pilot injector plays a crucial role in this process, as it generates a very energetic flame and a hot gas pocket in the central recirculation zone, which in turn anchors the flame issued from the multipoint injection. Results of this section show the ability of our models to perform fully turbulent reactive two phase flows in complex geometries, and the analysis of physics linked to these phenomena.

6 Conclusions

LES was performed in a complex aeronautical burner dedicated to lean spray combustion which presents a complex injection system made of three air swirler stages and two liquid kerosene injections, a pilot injector and a multipoint system. The mesoscopic Euler approach developed in the AVBP compressible solver was used. The combustion of kerosene was modeled by a two-step reduced scheme and the interaction with turbulence was accounted for using the Thickened Flame model. Injection and evaporation being key phenomena, their modeling was first validated by comparison with experiments in academic configurations. The FIM-UR method was used to reproduce experiments of liquid kerosene injection through a pressure swirl atomizer. An improvement of the classical Abramzon–Sirignano evaporation model was proposed to account for the dependence of mixture thermodynamical properties on composition, and then tested in the reference experiment of an evaporating isolated n-heptane droplet. Both models showed good agreement with experiment and were then used for the two-phase reacting simulation of a multipoint injection burner. Despite its limitations and still many open modeling issues, LES and models defining injection and evaporation were able to reproduce the crucial role of the pilot injection to stabilise a flame despite the very lean global equivalence ratio. The flame structure analysis showed new behaviours compared to gas flames, mainly due to evaporation: non adiabaticity, change in equivalence ratio across the flame front, diffusion flame far downstream of the premixed flame due to a very rich, oxygen-free burnt gas pocket generated by the pilot spray. Obviously, some models such as injection must be improved, and more quantitative comparisons with experiment, together with LES using an Euler–Lagrange approach, are required to improve the analysis of the burner performances.

Acknowledgement Part of this research project has been supported by the European Community under contract number 210781-2 within the Marie Curie Initial Training Network of the 7th Framework Programme.

References

1. Yuan, L.L., Street, R.L., Ferziger, J.H.: Large-eddy simulations of a round jet in crossflow. *J. Fluid Mech.* **379**, 71–104 (1999)
2. Yang, K.S., Ferziger, J.H.: Large-eddy simulation of turbulent obstacle flow using a dynamic subgrid-scale model. *AIAA J.* **31**(8), 1406–1413 (1993)

3. Verzicco, R., Mohd-Yusof, J., Orlandi, P., Haworth, D.: Large Eddy Simulation in complex geometric configurations using boundary body forces. *AIAA J.* **38**(3), 427–433 (2000)
4. Riley, J.: Review of Large-Eddy Simulation of non-premixed turbulent combustion. *J. Fluids Eng.* **128**(2), 209–215 (2006)
5. Murota, T., Ohtsuka, M.: Large-Eddy Simulations of combustion oscillation in premixed combustor. In: International Gas Turbine and Aeroengine Congress & Exposition, ASME Paper, vol. 99-GT-274 (1999)
6. Itoh, Y., Taniguchi, N., Kobayashi, T., Tominaga, T.: Large Eddy Simulation of spray combustion in swirling flows. In: ASME FEDSM, Honolulu, Hawaii, USA (2003)
7. Giffen, E., Muraszew, A.: Atomization of Liquid Fuels. Chapman & Hall, London (1953)
8. Spalding, D.B.: The combustion of liquid fuels. In: 4th Symp. (Int.) on Combustion, pp. 847–864. The Combustion Institute, Pittsburgh (1953)
9. Desoutter, G., Cuenot, B., Habchi, C., Poinso, T.: Interaction of a premixed flame with a liquid fuel film on a wall. *Proc. Combust. Inst.* **30**, 259–267 (2005)
10. Brandt, M., Gugel, K.O., Hassa, C.: Experimental investigation of the liquid fuel evaporation in a premix duct for lean premixed and prevaporized combustion. *J. Eng. Gas. Turbul. Power* **119**, 815–821 (1997)
11. Caraeni, D., Bergstrom, C., Fuchs, L.: Modeling of liquid fuel injection, evaporation and mixing in a gas turbine burner using large eddy simulation. *Flow Turbul. Combust.* **65**, 223–244 (2000)
12. Chiu, H.H., Croke, E.J.: Group combustion of liquid fuel sprays. Energy Technology Lab 81–2. University of Illinois, Chicago (1981)
13. Nakamura, M., Akamatsu, F., Kurose, R., Katsuki, M.: Combustion mechanism of liquid fuel spray in a gaseous flame. *Phys. Fluids* **17**, 123301 (2005)
14. Sornek, R.J., Dobashi, R., Hirano, T.: Effect of turbulence on vaporization, mixing, and combustion of liquid-fuel sprays. *Combust. Flame* **120**(4), 479–491 (2000)
15. Imaoka, R.T., Sirignano, W.A.: A generalized analysis for liquid-fuel vaporization and burning. *Int. J. Heat Mass Transfer* **48**, 4342–4353 (2005)
16. Menard, T., Tanguy, S., Berlemont, A.: Coupling level set/vof/ghost fluid methods: validation and application to 3d simulation of the primary break-up of a liquid jet. *Int. J. Multiphase Flow* **33**, 510–524 (2007)
17. Fuster, D., Bagné, A., Boeck, T., Moynea, L.L., Leboissetier, A., Popinet, S., Raya, P., Scardovelli, R., Zaleski, S.: Simulation of primary atomization with an octree adaptive mesh refinement and VOF method. *Int. J. Multiphase Flow* **35**, 550–565 (2009)
18. Zuzio, D., Estivaleres, J.: An efficient block parallel AMR method for two phase interfacial flow simulations. *Comput. Fluids* **44**, 339–357 (2011)
19. Boileau, M., Pascaud, S., Riber, E., Cuenot, B., Gicquel, L., Poinso, T., Cazalens, M.: Investigation of two-fluid methods for Large Eddy Simulation of spray combustion in gas turbines. *Flow Turbul. Combust.* **80**(3), 291–321 (2008)
20. Apte, S., Mahesh, K., Moin, P.: Large-eddy simulation of evaporating spray in a coaxial combustor. *Proc. Combust. Inst.* **32**(2), 2247–2256 (2009)
21. Sanjosé, M., Senoner, J., Jaegle, F., Cuenot, B., Moreau, S., Poinso, T.: Fuel injection model for Euler–Euler and Euler–Lagrange Large-Eddy Simulations of an evaporating spray inside an aeronautical combustor. *Int. J. Multiphase Flow* **37**, 514–529 (2011)
22. Hirschfelder, J.O., Curtiss, F., Bird, R.B.: Molecular Theory of Gases and Liquids. Wiley (1964)
23. Poinso, T., Veynante, D.: Theoretical and Numerical Combustion. R.T. Edwards (2001)
24. Ducros, F., Ferrand, V., Nicoud, F., Weber, C., Darracq, D., Gacherrieu, C., Poinso, T.: Large-eddy simulation of shock-turbulence interaction. *J. Comput. Phys.* **152**, 517–549 (1999)
25. Smagorinsky, J.: General circulation experiments with the primitive equations: 1. The basic experiment. *Mon. Weather Rev.* **91**, 99–164 (1963)
26. Février, P., Simonin, O., Squires, K.: Partitioning of particle velocities in gas-solid turbulent flows into a continuous field and a spatially uncorrelated random distribution: theoretical formalism and numerical study. *J. Fluid Mech.* **533**, 1–46 (2005)
27. Simonin, O.: Gaz particules, Cours d'options, Ecole Nationale Supérieure d'Electrotechnique, d'Electronique, d'Informatique, d'Hydraulique et des Télécommunications (2002)
28. Riber, E., Moureau, V., García, M., Poinso, T., Simonin, O.: Evaluation of numerical strategies for LES of two-phase reacting flows. *J. Comput. Phys.* **228**, 539–564 (2009)
29. Moreau, M., Simonin, O., Bédard, B.: Development of gas-particle Euler–Euler LES approach: a priori analysis of particle sub-grid models in homogeneous isotropic turbulence. *Flow Turbul. Combust.* **84**, 295–324 (2010)
30. Schiller, L., Nauman, A.: A drag coefficient correlation. *VDI Zeitung* **77**, 318–320 (1935)

31. Colin, O., Rudgyard, M.: Development of high-order taylor-galerkin schemes for unsteady calculations. *J. Comput. Phys.* **162**(2), 338–371 (2000)
32. Poinso, T., Lele, S.: Boundary conditions for direct simulations of compressible viscous flows. *J. Comput. Phys.* **101**(1), 104–129 (1992)
33. Lefebvre, A.H.: Atomization and sprays. In: *Combustion*. Hemisphere Publishing/Taylor & Francis (1989)
34. Yang, J.T., Chen, A.C., Yang, S.H., Huang, K.J.: Flow analysis of spray patterns of pressure-swirl micro atomizers. In: *Pacific Symposium on Flow Visualization and Image Processing*, vol. 4052. National Tsing Hua University (2003)
35. Nomura, H., Ujiie, Y., Rath, H.J., Sato, J., Kono, M.: Experimental study on high-pressure droplet evaporation using microgravity conditions. *Proc. Combust. Inst.* **26**, 1267–1273 (1996)
36. Chauveau, C., Halter, F., Lalonde, A., Gokalp, I.: An experimental study on the droplet vaporization: effects of heat conduction through the support fiber. In: *ILASS*, 4-1. Como Lake, Italy (2008)
37. Sanjosé, M.: Evaluation de la méthode Euler-Euler pour la simulation aux grandes échelles des chambres à carburant liquide, Ph.D. thesis, INP Toulouse (2009)
38. Sierra, P.S.: Modeling the dispersion and evaporation of sprays in aeronautical combustion chambers. Ph.D. thesis, Institut National Polytechnique de Toulouse (2012)
39. Abramzon, B., Sirignano, W.A.: Droplet vaporisation model for spray combustion calculations. *Int. J. Heat Mass Transfer* **9**, 1605–1618 (1989)
40. Ranz, W.E., Marshall, W.R.: Evaporation from drops. *Chem. Eng. Prog.* **48**(4), 173 (1952)
41. Hubbard, G.L., Denny, V.E., Mills, A.F.: Droplet evaporation: effects of transient and variable properties. *Int. J. Heat Mass Transfer* **18**, 1003–1008 (1975)
42. Goodwin, D.G.: Cantera C++ Users Guide. <http://sourceforge.net/projects/cantera>. Version 1.80 (01 01 2011) (2002). Accessed 1 Jan 2011
43. Bird, R.B., Stewart, W.E., Lighfoot, E.N.: *Transport Phenomena*. Wiley, New York (1960)
44. Franzelli, B., Riber, E., Sanjosé, M., Poinso, T.: A two-step chemical scheme for Large-Eddy Simulation of kerosene-air flames. *Combust. Flame* **157**(7), 1364–1373 (2010)
45. Colin, O., Ducros, F., Veynante, D., Poinso, T.: A thickened flame model for large eddy simulations of turbulent premixed combustion. *Phys. Fluids* **12**(7), 1843–1863 (2000)
46. Jaegle, F., Senoner, J.M., Garcia, M., Bismes, F., Lecourt, R., Cuenot, B., Poinso, T.: Lagrangian and eulerian simulations of evaporating fuel spray in an aeronautical multipoint injector. *Proc. Combust. Inst.* **33**, 2099–2107 (2011)
47. Yamashita, H., Shimada, M., Takeno, T.: A numerical study on flame stability at the transition point of jet diffusion flame. In: *26th Symp. Int. on Combustion*, pp. 27–34. The Combustion Institute, Pittsburgh (1996)